

Research Article

Prediction of Aerosol Particle Size Distribution Based on Neural Network

Yali Ren,^{1,2} Jiandong Mao ,^{1,2} Hu Zhao,^{1,2} Chunyan Zhou,^{1,2} Xin Gong,^{1,2} Zhimin Rao,^{1,2} Qiang Wang,^{1,2} and Yi Zhang^{1,2}

¹School of Electrical and Information Engineering, North Minzu University, North Wenchang Road, Yinchuan 750021, China

²Key Laboratory of Atmospheric Environment Remote Sensing of Ningxia, North Wenchang Road, Yinchuan 750021, China

Correspondence should be addressed to Jiandong Mao; mao-jiandong@163.com

Received 18 December 2019; Accepted 20 May 2020; Published 6 June 2020

Academic Editor: Enrico Ferrero

Copyright © 2020 Yali Ren et al. This is an open access article distributed under the Creative Commons Attribution License, which permits unrestricted use, distribution, and reproduction in any medium, provided the original work is properly cited.

Aerosol plays a very important role in affecting the earth-atmosphere radiation budget, and particle size distribution is an important aerosol property parameter. Therefore, it is necessary to determine the particle size distribution. However, the particle size distribution determined by the particle extinction efficiency factor according to the Mie scattering theory is an ill-conditioned integral equation, namely, the Fredholm integral equation of the first kind, which is very difficult to solve. To avoid solving such an integral equation, the BP neural network prediction model was established. In the model, the aerosol optical depth obtained by sun photometer CE-318 and kernel functions obtained by Mie scattering theory were used as the inputs of the neural network, particle size distributions collected by the aerodynamic particle sizer APS 3321 were used as the output, and the Levenberg–Marquardt algorithm with the fastest descending speed was adopted to train the model. For verifying the feasibility of the prediction model, some experiments were carried out. The results show that BP neural network has a better prediction effect than that of the RBF neural network and is an effective method to obtain the aerosol particle size distribution of the whole atmosphere column using the data of CE-318 and APS 3321.

1. Introduction

As an important part of the atmosphere-earth system, aerosols affect the earth-atmosphere radiation budget through direct effects (scattering and absorption of solar radiation) and indirect effects (mainly caused by changes in cloud characteristics) [1]. Therefore, changes in aerosol properties can affect many aspects of the atmosphere [2], such as climate, environment, rainfall, and visibility. In the study of atmospheric aerosols, particle size distribution (PSD) is a representative parameter of the atmospheric aerosol physical characteristics, which describes the size distribution of particles with different diameters in the atmosphere. For example, PM_{2.5} and PM₁₀, which can affect human health, refer to the particles with 2.5 and 10 μm or less in diameter. Therefore, to fully understand the characteristics of aerosols, it is necessary to study the PSD.

There are some methods for obtaining aerosol PSD. In recent years, the retrieval methods for PSD based on remote

sensing have become more and more mature, which are divided into the active remote sensing and passive remote sensing. The passive remote sensing refers to the detection system without a radiation source in the remote sensing system. In other words, the detection instrument acquires and records the electromagnetic or light wave emitted or reflected by the target object itself from natural radiation sources (such as the sun) to achieve atmospheric detection, such as sun photometer and particle size spectrometer. Most measurements are based on the different attenuation of solar radiation by different scales particles, among which the extinction method is the earliest and most widely applied [3]. In 1980, Zhao et al. used a multiband photometer for inversion of aerosol particle size and achieved better results in Beijing. In 2000, Vito Vitale employed the IR-RAD sun photometer to measure aerosol optical depth (AOD), calculated root-mean-square of the difference between measured AOD and assumed AOD under different complex refractive index, and used the minimum root-mean-square

to invert the PSD and obtained better fitting effect [4]. From 2002 to 2013, Che et al. used the Chinese Aerosol Remote Sensing Network (CARSNET) to make long-term measurements of the AOD (440 nm) and the Ångström exponent (AE, 440–870 nm) at 50 sites and analyzed the AOD and AE obtained. It is concluded that the AODs show decreasing trends from 2006 to 2009 but increased ~ 0.03 per year from 2009 to 2013 [5]. In 2019, Che et al. made multiyear observations of aerosol microphysical and optical properties obtained from ground remote sensing of 50 aerosol remote sensing sites (CARSNET) in China. The variation trends of the average effective radius, AOD (440 nm), AE (440 nm–870 nm), single scattering albedo (440 nm), and average direct aerosol radiation effect in typical remote, rural, and urban areas of China were obtained. The results play an important role in understanding aerosol climate impacts and regional environmental pollution and also provide useful information for satellite validation and the improvement of climate modelings [6]. In 2019, Fan et al. observed and analyzed the atmospheric optical properties of Shouxian in winter by using solar photometer, turbidimeter, and particulate matter detector. The results showed that, with the increase of aerosol content, the particulate matter content increased and the AOD, scattering coefficient, and single scattering albedo increased, as well as the aerosol wavelength index and atmospheric turbidity coefficient [7].

Active remote sensing refers to a remote sensing system that transmits a certain form of electromagnetic or light wave to the target from an artificial radiation source on a remote sensing platform and then receives and records its return signals by the sensor. Its advantage is the fact that it does not depend on solar radiation, can work day and night, and can actively choose the emission wavelength and mode according to the different detection purposes [8]. For example, the multiwavelength LiDAR with 355, 532, and 1064 nm can detect the aerosols extinction coefficient and further retrieve the aerosol PSD by solving the Fredholm integral equation of first kind [9]. The relationship between the aerosol extinction coefficient and the PSD is the Fredholm integral equation of the first kind and can be expressed as follows [10, 11]:

$$\begin{aligned}\tau(\lambda) &= \int_0^{z_M} dz \int_0^{r_M} dr \pi r^2 n(r, z) Q_{\text{ext}}(r, \lambda, m) \\ &= \int_{r_0}^{r_M} \pi r^2 Q_{\text{ext}}(r, \lambda, m) n(r) dr,\end{aligned}\quad (1)$$

where $Q_{\text{ext}}(r, \lambda, m)$ is the kernel function, namely, extinction efficiency factor; m is the complex refractive index of aerosol particles; r is the radius; λ is wavelength; $\tau(r)$ is the AOD; and $N(r)$ is the aerosol PSD of whole atmosphere column. Through solving this integral equation, the aerosol particle distribution $n(r)$ can be inverted.

Since the Fredholm integral equation of the first kind is ill-posed and unstable, in order to solve such equations, some technology, including regularization, Phillips–Twomey's regularization, Tikhonov's smooth regularization, and iterative

methods were proposed [12]. Phillips added the smooth factors and smooth matrices and constructed the corresponding linear inversion techniques to solve the integral equation. However, if initial fast-change functions and smooth matrix selected are unreasonable, the solution will fail [13]. Twomey also introduced a smoothing factor into the linear inversion technique and enhanced the constraint of the inversion results when inverting the PSD from extinction coefficients [14]. Nguyen proposed an improved antifold algorithm to invert particle concentration and size distribution by solving the Fredholm integral equation from extinction coefficient measurements of multiple wavelengths [15]. Mao employed the particle swarm optimization (PSO) algorithm to retrieve the aerosols size distribution by using AODs taken by a sun photometer CE-318 in the Yinchuan area and compared with the simple genetic algorithm (SGA). The results showed that the PSO retrieval algorithm was appropriate for different weather conditions and had good applicability [16].

In this paper, in order to avoid solving the integral equation, the BP neural network prediction model was employed, in which the AODs obtained by the CE-318 sun photometer and kernel function obtained by Mie scattering theory were used as the inputs of BP neural network, and the PSD collected by the APS-3321 aerodynamic particle sizer was used as the output. After training neural networks by using a large amount of historical data, the current measurement AODs and kernel functions were inputted; the aerosol PSD of the whole atmosphere column can be predicted well. The data sources and Mie scattering theory are described in Section 2 the retrieval model based on the BP neural network is discussed in Section 3 The experiments and results are analyzed in Section 4 The main conclusions are presented in Section 5

2. Data Sources and Mie Scattering Theory

2.1. Aerosol Optical Depth

2.1.1. Sun Photometer. Sun photometer is a passive atmospheric remote sensing instrument that can directly detect solar radiation and conduct sky scanning. It has two optical probes, one is employed for sky radiation measurement with a transparent mirror and the other is used for measuring direct solar radiation without a concentrator lens. The measured solar radiation data can be used to calculate the atmospheric transmittance, AOD, total atmospheric vapor column, and total ozone amount. The data of sky radiation scanning data can be used to invert the aerosol PSD, phase function, and other atmospheric optical parameters. AODs independent of atmospheric visibility are obtained by integrating the extinction coefficient of the whole atmosphere column, which can indicate the atmospheric aerosol load. Meanwhile, multiwavelength AOD inversion can provide aerosol size information [17]. In this paper, a CE-318 automatic sun photometer produced by CIMEL company is employed for goal, which was set up at the roof of No. 17 teaching building of North Minzu University (106° 29' E, 38° 13' N). Table 1 lists the functions of various bands of CE-318.

TABLE 1: The functions of various bands of CE-318.

Center wavelength(nm)	340 380	440 500 670 870 1020	1640
The band width(nm)	2 2	10 10 10 10 10	60
Functions of each band	Measure ozone and uv	Measurement of aerosol	Measure atmospheric aerosol sensitivity

2.1.2. *Calculation of AOD.* According to Beer's law, the total optical depth of the atmosphere is expressed by

$$\tau_{\text{total}}(\lambda) = \tau_{\text{atm}}(\lambda) + \tau_{\text{oz}}(\lambda) = \tau_r(\lambda) + \tau_a(\lambda) + \tau_{\text{oz}}(\lambda), \quad (2)$$

where $\tau_r(\lambda)$ is the atmospheric molecular Rayleigh scattering optical depth; $\tau_a(\lambda)$ is the AOD; τ_{oz} is the optical depth of the ozone. For CE-318 the ozone is considered from 340 to 1020 nm, but it should be pointed out that the inversion of the AODs in all bands does not consider the effect of water vapor. In fact, according to Bouguer exponential extinction law, for monochromatic light radiation, the direct solar radiation signal near the water vapor absorption band of 936 nm does not meet Bouguer's law. Moreover, there is no obvious water vapor absorption band in the band used in this paper, so the influence of water vapor can be ignored.

The optical depth of the atmospheric molecule Rayleigh scattering is calculated by [18]

$$\tau_r(\lambda) = 0.008569\lambda^{-4} \left(1 + 0.0113\lambda^{-2} + 0.00013\lambda^{-4}\right) \frac{P}{1013.25}, \quad (3)$$

where P is the atmospheric pressure of the observation point during the observation period (unit: hPa) and the constant of 1013.25 is the American standard atmospheric pressure (unit: hPa).

The optical depth of zone is calculated by

$$\tau_{\text{oz}}(\lambda) = a_{\text{oz}}(\lambda) \frac{U}{1000}, \quad (4)$$

where $a_{\text{oz}}(\lambda)$ is the absorption coefficient of ozone. U is the ozone content (unit DU).

In the 340–1640 nm bands, the contribution of the emitted radiation from the Earth-atmosphere system can be omitted, which does not consider the diffuse radiation caused by multiple scatterings. According to the Beer–Bouguer–Lambert theorem, the monochromatic direct irradiance of the sun through the Earth's atmosphere to the ground $E(\lambda)$ can be expressed as

$$E(\lambda) = E_0(\lambda) \cdot d_s \cdot \exp(-m(\tau_{\text{atn}}(\lambda) + \tau_{\text{oz}}(\lambda))), \quad (5)$$

where $E_0(\lambda)$ is the direct monochromatic irradiance of the sun at the top of the Earth's atmosphere at the average distance between the sun and the Earth. d_s is the sun-Earth distance correction factor. m is the atmospheric mass number. $\tau_{\text{atn}}(\lambda)$ is the atmospheric optical depth, mainly including the atmospheric molecular Rayleigh scattering optical depth and AOD, regardless of the influence of absorbing gas.

Since the detection element of sun photometer is linear and there is a linear relationship between the DN value of the

instrument's output and the radiation of the sun, according to the Beer–Bouguer–Lambert theorem, one can obtain [19]

$$\frac{E_0(\lambda)}{E(\lambda)} = \frac{\text{DN}_0(\lambda)}{\text{DN}(\lambda)}, \quad (6)$$

$$\tau_{\text{total}}(\lambda) = \frac{1}{m} \ln \frac{\text{DN}_0(\lambda) d_s}{\text{DN}(\lambda)}. \quad (7)$$

Therefore, the AOD is written by

$$\tau_a(\lambda) = \tau_{\text{total}}(\lambda) - \tau_r(\lambda) - \tau_{\text{oz}}(\lambda). \quad (8)$$

2.2. *Mie Scattering Theory.* When the size of the scattering particles is similar to or greater than the incident wavelength, the Mie scattering is dominant. The uniform sphere scattering is mainly described by Mie scattering theory [20]. Mie scattering is based on Maxwell's equations; the expressions of scattering cross section, extinction cross section, and absorption cross section can be obtained when the light is linearly polarized light. The corresponding efficiency factors of scattering, extinction, and absorption are given by

$$\begin{aligned} Q_{\text{sca}} &= \frac{2}{x^2} \sum_{n=1}^{\infty} (2n+1) (|a_n|^2 + |b_n|^2), \\ Q_{\text{ext}} &= \frac{2}{x^2} \sum_{n=1}^{\infty} (2n+1) \text{Re}(a_n + b_n), \\ Q_b &= \frac{1}{x^2} \left| \sum_{n=1}^{\infty} (2n+1) (-1)^n (a_n - b_n) \right|^2, \end{aligned} \quad (9)$$

where

$$\begin{aligned} a_n(x, m) &= \frac{m\psi_n(mx)\psi_n''(x) - \psi_n(x)\psi_n'(mx)}{m\psi_n(mx)\zeta_n'(x) - m\zeta_n(x)\psi_n'(mx)}, \\ b_n(x, m) &= \frac{\psi_n(mx)\psi_n''(x) - m\psi_n(x)\psi_n'(mx)}{\psi_n(mx)\zeta_n'(x) - m\zeta_n(x)\psi_n'(mx)}, \end{aligned} \quad (10)$$

where $\psi_n(\alpha) = \sqrt{\pi\alpha/2} J_{n+(1/2)}(\alpha)z$, $\xi_n(\alpha) = \sqrt{\pi\alpha/2} H_{n+(1/2)}^{(2)}(\alpha)$; $J_{n+(1/2)}(\alpha)$ is the Bessel function; $H_{n+(1/2)}^{(2)}(\alpha)$ is the Hankel function of the second kind; and α is the scale parameter, $\alpha = 2\pi r/\lambda$. Ψ' and ξ' are the derivatives of Ψ and ξ , respectively. m is the complex index, $m = m' + i''$. a_n and b_n are the Mie coefficients. $x = 2\pi/\lambda$ is the wavenumber. When $0.1 < \alpha < 50$, $r \approx \lambda$, the scattering is coarse scattering or Mie scattering. The complex refractive index of aerosols is the main optical parameter of absorbing media and is usually a complex number. The real part m' is related to the type of light scattering, and the image part m'' is related to electromagnetic waves. The complex refractive index depends on its chemical composition and wavelength, which is

different for different particles. The Yinchuan area, surrounded by four deserts, has a high altitude, a dry climate, and frequent dusty weather, which is a typical semiarid climate in northwest China. In this paper, $m = 1.55 + 0.01i$ is selected to invert the extinction factor [17]. By Mie scattering theory, the extinction efficiency factors of the different wavelengths, including 1064, 1020, 870, 670, 550, 440, 380, and 340 nm, can be obtained.

Figure 1 shows the efficiency factors of extinction and scattering obtained from the Mie scattering theory. The x -coordinate represents the scale factor, and the y -coordinate denotes the efficiency factors of extinction and scattering, respectively. It can be seen that the efficiency factors of extinction and scattering of the wavelength of 340 nm oscillate before other wavelengths, while the 1064 nm has the largest oscillation amplitude. The curve shifts to the right along with the scale parameters and finally tends to be stable around 2.

2.3. Aerodynamic Particle Sizer APS 3321. In this paper, the aerodynamic particle size spectrometer APS 3321 produced by TSI company is adopted. For APS 3321 after sample gas is accelerated through the nozzle, particles of different sizes obtain different initial speeds. When passing through the monitoring area, particles of different sizes generate different optical scattering signals to two parallel laser beams. By converting the signals into electronic pulse signals, the time between the wave peaks of pulse signals (i.e., the time when the particles fly between the two laser beams) provides the information of particle aerodynamic size. A single high-speed processor is used to detect the flight time of a single particle in the accelerated airflow to obtain the aerosol PSD [21]. The particle size range is from 0.5 to 20 microns, which corresponds to 52 particle size channels. The APS 3321 can not only detect the particle concentration in the atmosphere including the number concentration, mass concentration, and size distribution but also check the size distribution of different particle size ranges through the AIM software. Also it can measure the average concentration.

Figure 2(a) shows the aerosol particle distributions on July 25, 2019. It is clear that the aerosol particle number concentration in the morning is higher than that in the afternoon, and the aerosol particle number is relatively higher at around 8:30 AM, 12:00 AM, 7:00 PM, and 11:00 PM, which is closely related to people's daily life. This trend shows that the aerosol particle number concentration is consistent with real life, so it is reasonable to use these data for training and prediction. Figure 2(b) shows the aerosol particle distribution at the same moment under different weather conditions, including sunny days, hazy days, and dusty weather. The number of coarse particles in the dusty day is more than that in sunny days. The concentration of small particles ($<0.723 \mu\text{m}$) in the hazy day is higher than that in the dusty day but higher than that in sunny days. Also, it found that the concentration of the night is higher than that of the day; this is because the temperature difference between day and night is relatively large, and the temperature of high

altitude is higher than that of ground; air near the ground will carry pollutants up, so at this time, the aerosol particle number concentration is bigger when the sun rises, the surface temperature rises, and the particle concentration will start to decline.

3. The Neural Network Prediction Model

BP neural network is a feed-forward network, trained by the error backpropagation algorithm [22]. The three-layer network is the most simple structure for the BP neural network, including the input layer, hidden layer, and output layer. The training process of the BP network includes forward transmission of signals and backpropagation of errors. In forward transmission, input signals are processed layer by layer from the input layer through the hidden layer to the output layer. The state of each layer affects only the state of the next layer. If the expected output is not available at the output layer, the backpropagation process is performed, in which the network weight and threshold are adjusted according to the prediction error. After the above-repeated iterations, the predicted network output gradually approaches the expected output. However, the convergence rate of the BP neural network is particularly slow and easy to fall into the local minimum. In this paper, the Levenberg–Marquardt (LM) algorithm with the fastest descent speed is adopted as the training method, which has a fast gradient descent speed and makes the network not easy to fall into the local minimum [23, 24]. LM algorithm is a nonlinear optimization method between Newton method and gradient drop method, which is not sensitive to over parametric problem, and can effectively deal with redundant parameters and greatly reduce the chance of cost function falling into local minimum value. The key of it is to use the model function to treat the estimation parameter vector and to do linear approximation in its field, which ignores the derivative items above the second order and thus convert into a linear least square. Therefore LM algorithm has the advantage of fast convergence speed. Also the transfer function from the input layer to the hidden layer selects $\text{logsig}(x)$, and the transfer function from the hidden layer to the output layer selects $\text{tansig}(x)$.

The hidden layer is the main part of the neural network and the node number of the hidden layer can be determined by

$$l = \sqrt{n + m} + a, \quad (11)$$

where l , n , and m are the node number of hidden, input, and output layers, respectively, and a is the adjustment constant from 1 to 10. According to equation (11), the number of hidden layer nodes is selected as 10. In this paper, the AODs of eight wavelengths obtained by the sun photometer at 1640, 1020, 870, 670, 500, 440, 380, and 340 nm were taken as input nodes from 500 sets of data from June to July 2019. The extinction efficiency factor of the above wavelengths obtained from the Mie scattering theory was also taken as input nodes. So the input nodes were $16 * 500$. The output nodes corresponded to 52-channel measured value of the APS 3321. Double hidden layers structure is selected. When the

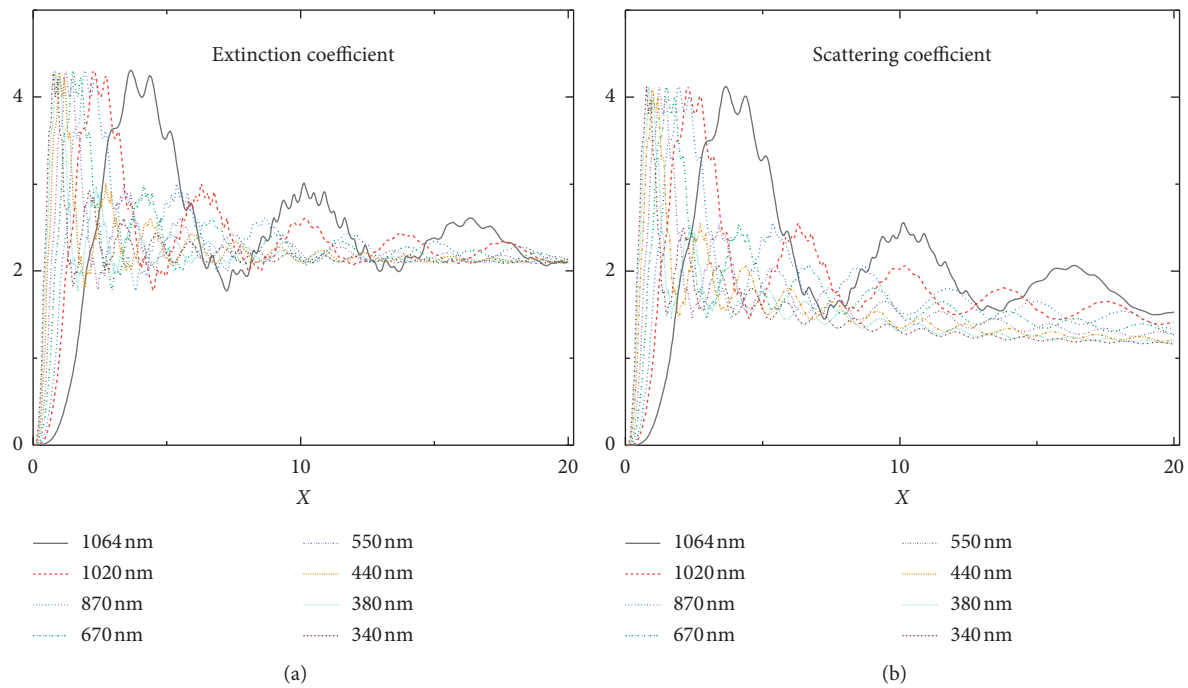


FIGURE 1: The efficiency factors of extinction and scattering of Mie scattering.

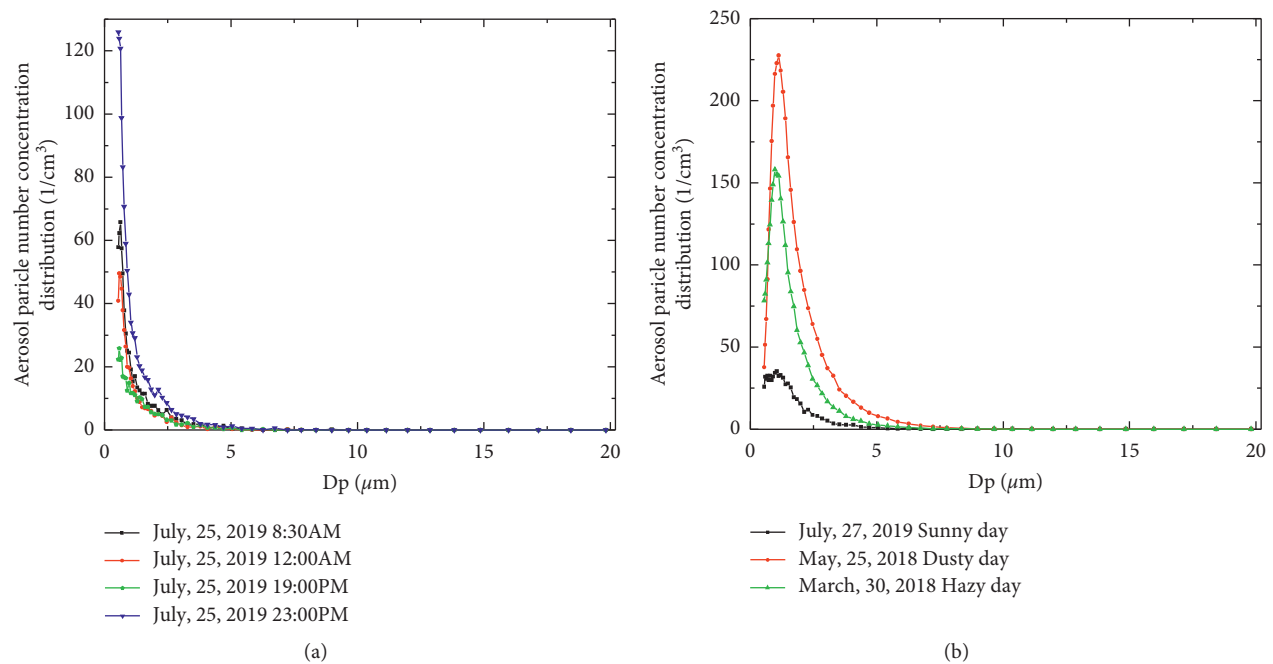


FIGURE 2: (a) The aerosol PSD on July 25, 2019 and (b) at the same moment under different weather conditions.

number of the first hidden layers is 10, the prediction time is shortest and the error is smallest. Therefore, the 16-10-52-52 four-layer structures are adopted for the BP neural network prediction model. Figure 3 shows the structure diagram of the BP neural network prediction model. Figure 4 shows the prediction flow chart of aerosol PSD based on BP neural network.

4. Experiment and Result Analysis

4.1. Data Preprocessing. In order to improve the accuracy of prediction and avoid network errors caused by large differences in the magnitude of input and output data, the normalization process of the original data is necessary [25]:

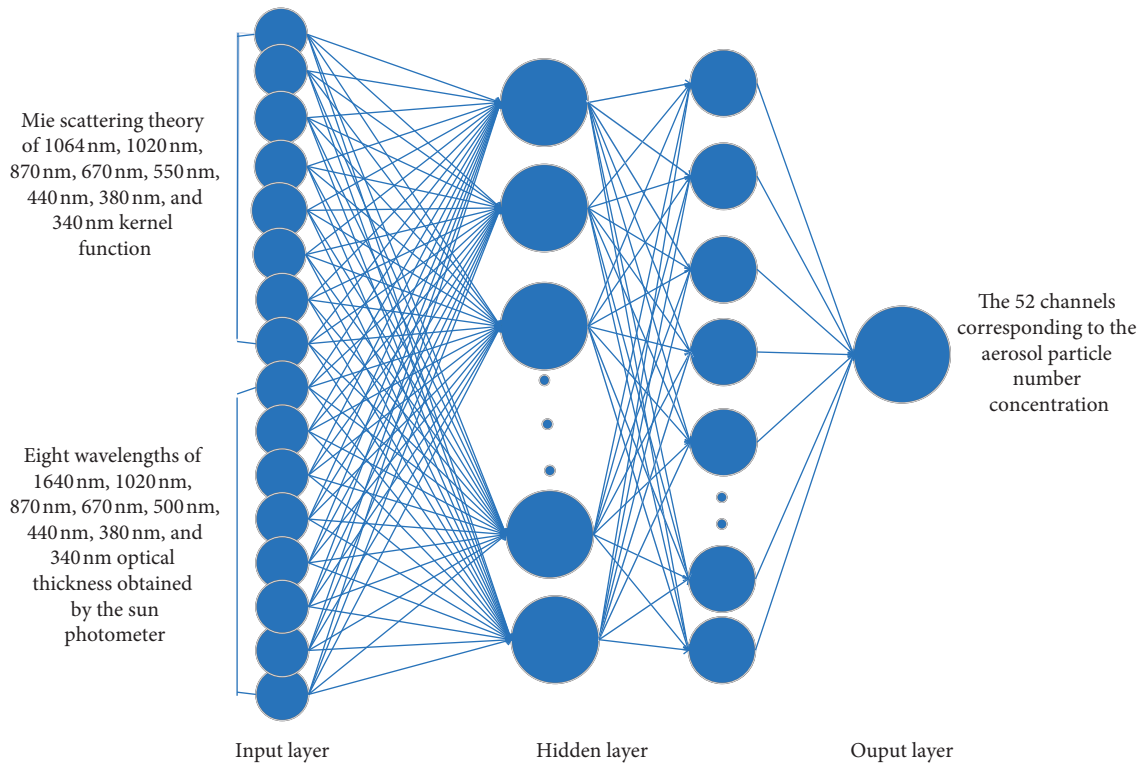


FIGURE 3: The structure diagram of the BP neural network prediction model.

$$x'' = \frac{x_k - x_{\min}}{x_{\max} - x_{\min}}, \quad (12)$$

where x_k is the original data obtained, x_{\max} represents the maximum value in the measured samples, and x_{\min} represents the minimum value in the measured samples. The prediction is carried out according to the flow chart shown in Figure 4. At the same time, in order to prove that there is no overfitting in the training process, the learning curve of BP neural network is shown in Figure 5. In the prediction process, learning rate, iteration number, target, and other parameters need to be adjusted to make the prediction results be best.

4.2. Prediction Result Analysis. To verify the feasibility of the proposed prediction model, some experiments were performed and the aerosol PSDs on summer sunny days, winter sunny days, and dusty days were measured, in which the PSD in sunny weather can be selected as the background value. There are 500 groups of measured aerosol PSDs taken by APS 3321 and AODs obtained by CE-318 are chosen, including from July 20, 2019, to July 25, 2019, for summer sunny days, August 25, 2018, for dusty day, and December 25, 2017, for winter sunny days. Among them there are 300 groups in sunny days, 100 groups in winter sunny day, and 100 groups in dusty day. Adopting the aerosol particle number concentration in winter is due to aerosol particle number concentration in winter being significantly higher than that of the summer, which may be due to the increase in pollutants caused by winter heating. In fact, in winter, due to

the relatively stable air structure in Northwest China, the pollutants discharged by heating are not easily diffused, which cause serious pollution. Also, due to the high number concentration of aerosol particles in dusty weather, the average number concentration is higher than that of sunny days.

It is as shown in the flow sequence of Figure 4, firstly, the input and output data sets are loaded, and the training data and prediction data are identified. Secondly, the input and output data are normalized. Then the network training is conducted; through forward calculation, the output aerosol particle number concentration is compared with that measured actually. If the output value does not meet the expected value, the backward calculation is carried out. Such training process will be repeated, until the output results meet the expected value or the number of cycles meets the requirements. After the network is trained well and the model parameters are determined, if the newly measured aerosol optical depth and kernel function are inputted to model, the predicted aerosol particle number concentration distribution will be obtained. When training the BP neural network, the correlation coefficient, average error, and mean square root error can be selected as the criteria for evaluating the prediction results.

Moreover, for the selection of the data set, the larger the training data of the neural network, the better the effect. However, if the training set is too large, the overfitting will occur. Generally speaking, in BP neural network, 90% of data is used for training and 10% for prediction. In this paper, 94% of the data is used for training. Because there is no clear requirement, 94% of

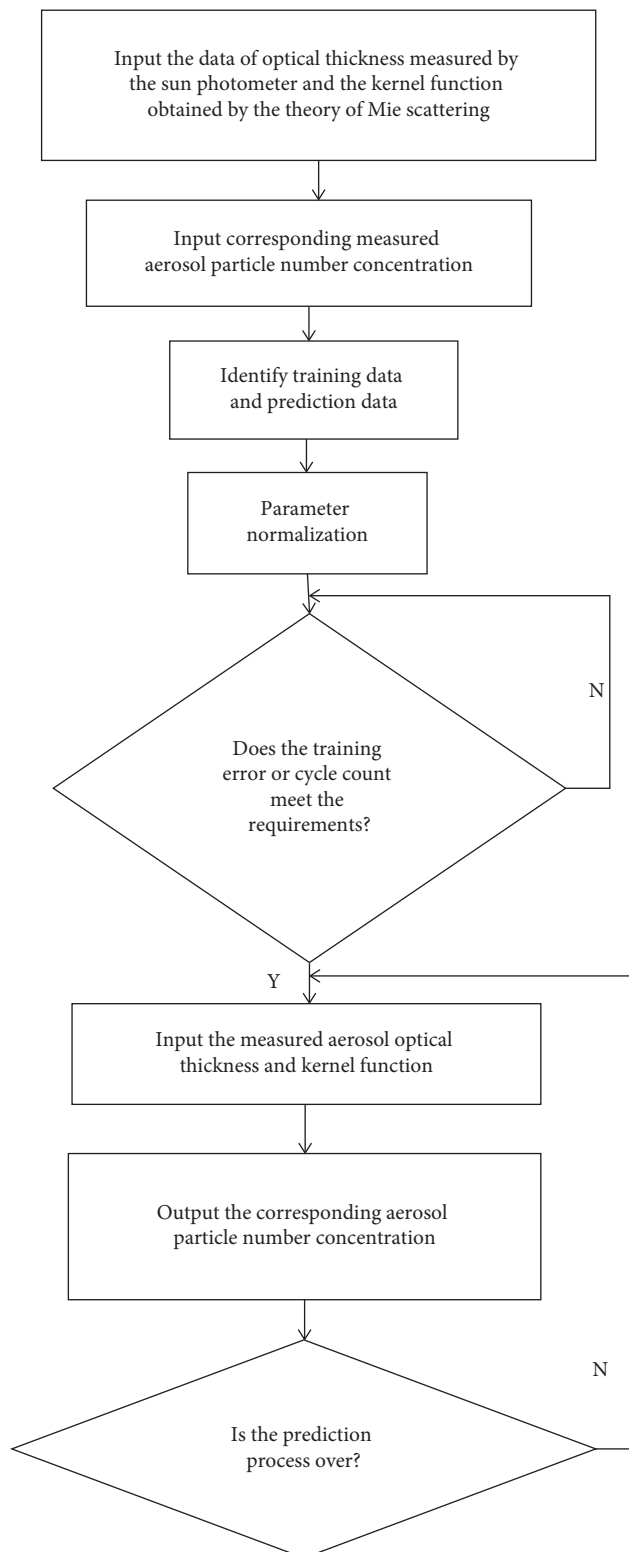


FIGURE 4: The prediction flow chart of aerosol PSD based on BP neural network.

the test set is also feasible. In fact, the BP neural network prediction model selects 470 sets as training data; among them, there are 282 sunny days in summer, 94 sunny days in winter, and 94 dusty days in spring. A total of 30 sets of

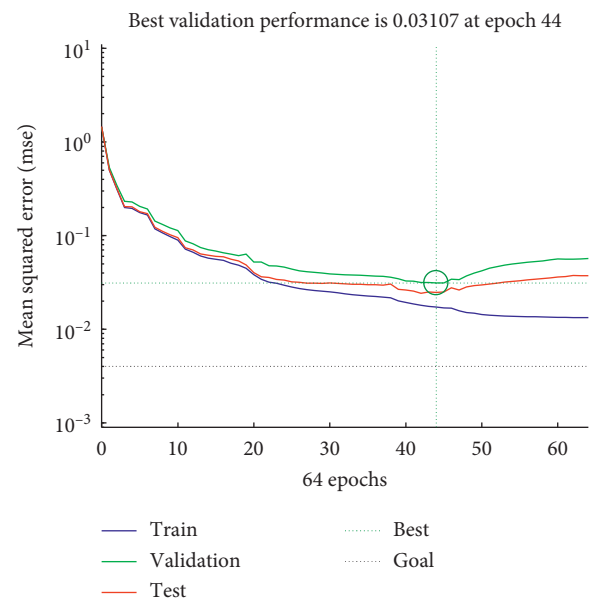


FIGURE 5: The BP neural network learning curve.

data are used for prediction: 18 sunny days in summer, 6 sunny days in winter, and 6 dusty days in spring. Figure 6 shows the comparison between prediction results and measured results on sunny, winter sunny days, and dusty days based on BP neural network. The number concentration unit is $1/\text{cm}^3$.

It can be seen from Figure 6 that, in the dusty day, the peak appears at the diameter of about $12\ \mu\text{m}$, which indicates that in dusty weather there was a significant amount of coarse particles. The concentration of aerosol particles in winter sunny day is significantly higher than that in summer sunny days. Figure 7 shows the prediction correlation relationship of BP neural network model, where the horizontal coordinate is the measured value of the aerosol particle number concentration, and the ordinate is the predicted value. It is clear that the correlation coefficient reaches 0.99009, which shows the prediction result is in good agreement with the measured result.

In order to verify the prediction effect of the BP neural network model, the radial base function (RBF) neural network model is also selected to predict aerosol PSD. As a good performance feed-forward neural network, the RBF neural network has the ability of arbitrarily accurate to close to any nonlinear function and obtains global approximation. In order to compare the two prediction models, the same input and output were used as the RBF neural network. Figure 8 shows the comparison between prediction results and measured results on summer sunny days, winter sunny days, and dusty days based on RBF neural network. Figure 9 shows the prediction correlation relationship of the RBF neural network prediction model, in which the correlation coefficient is 0.97925.

It can be seen from Figures 7 and 9 that BP neural network has a better fitting effect on the aerosol PSD compared with RBF neural network and has a small error between the measured value and the prediction value. In this

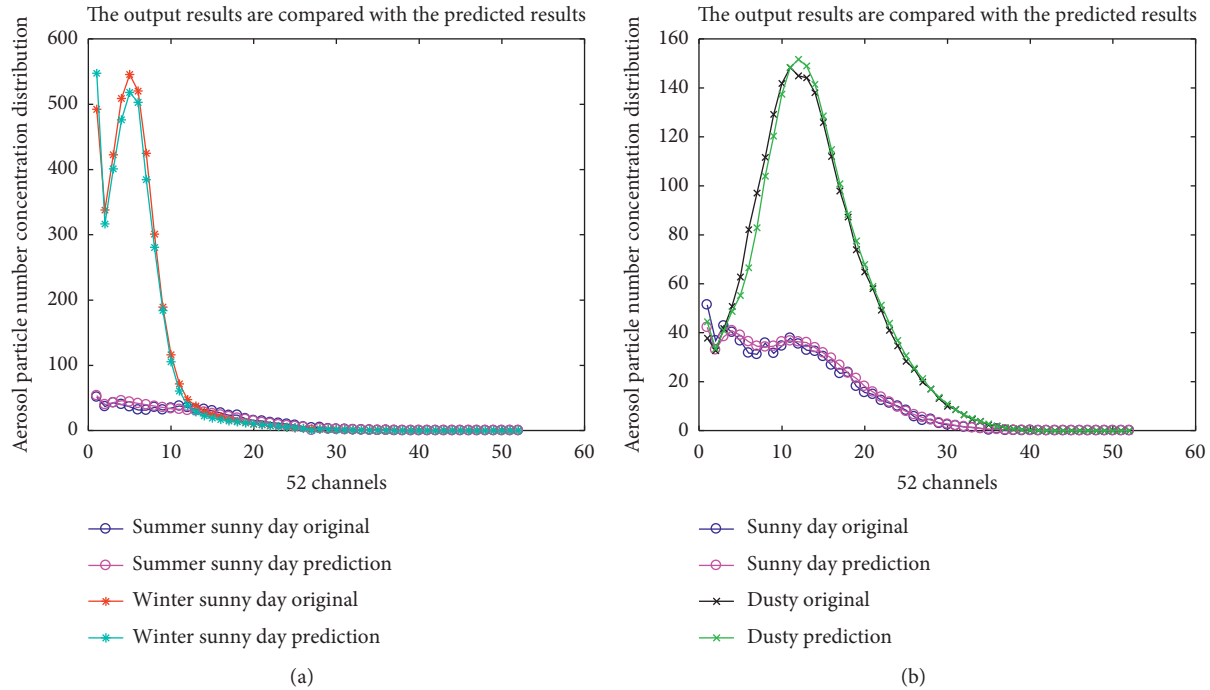


FIGURE 6: The comparison between prediction results and measured results on summer sunny days, winter sunny days, and dusty days based on BP neural network.

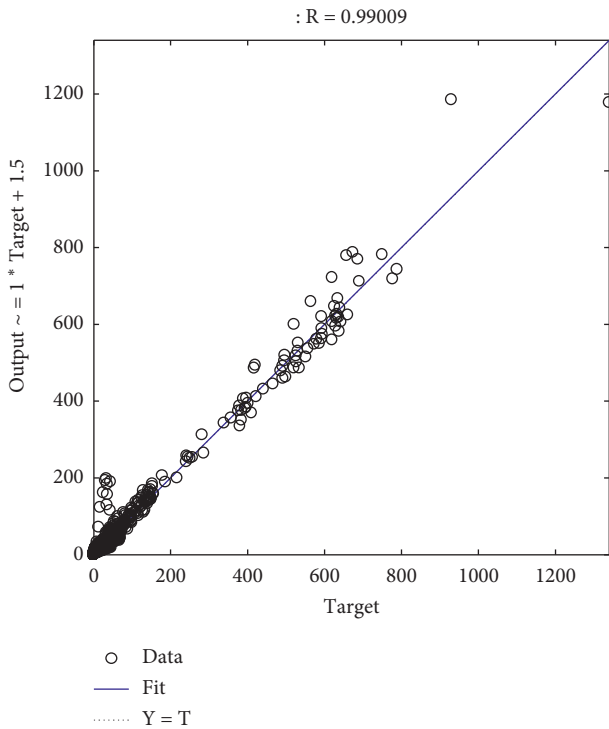


FIGURE 7: The prediction correlation relationship of BP neural network model.

paper, the average error and root-mean-square error are used to evaluate the model prediction error. The average error is written by

$$E = \frac{1}{n} \sum_{i=1}^n |f_i - Y_i|. \quad (13)$$

In this paper, the mean square error (MSE) is selected as the loss function of neural network. The MSE refers to the expected value of the square of the difference between the parameter estimate and the true value of the parameter. MSE can evaluate the degree of change in the data. The smaller the value of MSE, the better the accuracy of the prediction model in describing test data. The MSE is defined by

$$\text{MSE} = \frac{1}{n} \sum_{i=1}^N e_i^2. \quad (14)$$

The root-mean-square error is defined as [26]

$$R = \sqrt{\frac{\sum_{i=1}^N e_i^2}{n}}, \quad (15)$$

where f_i is the predicted value and Y_i is the measured value. $e = f_i - Y_i$. N is the number of predicted groups, which is 30 in this paper and $0 \leq i < 31$.

The performance comparisons between BP and RBF neural network are listed in Table 2.

From Table 2, compared to RBF neural network, the BP neural network has a better correlation relationship and has a smaller error. However, for BP neural network, the prediction time is twice as long as the RBF. This is because the Sigmoid function used by the BP network has global nature, which affects the output value in a large range of input values for each node, and the activation functions produce overlap and influence each other over a wide range of input values.

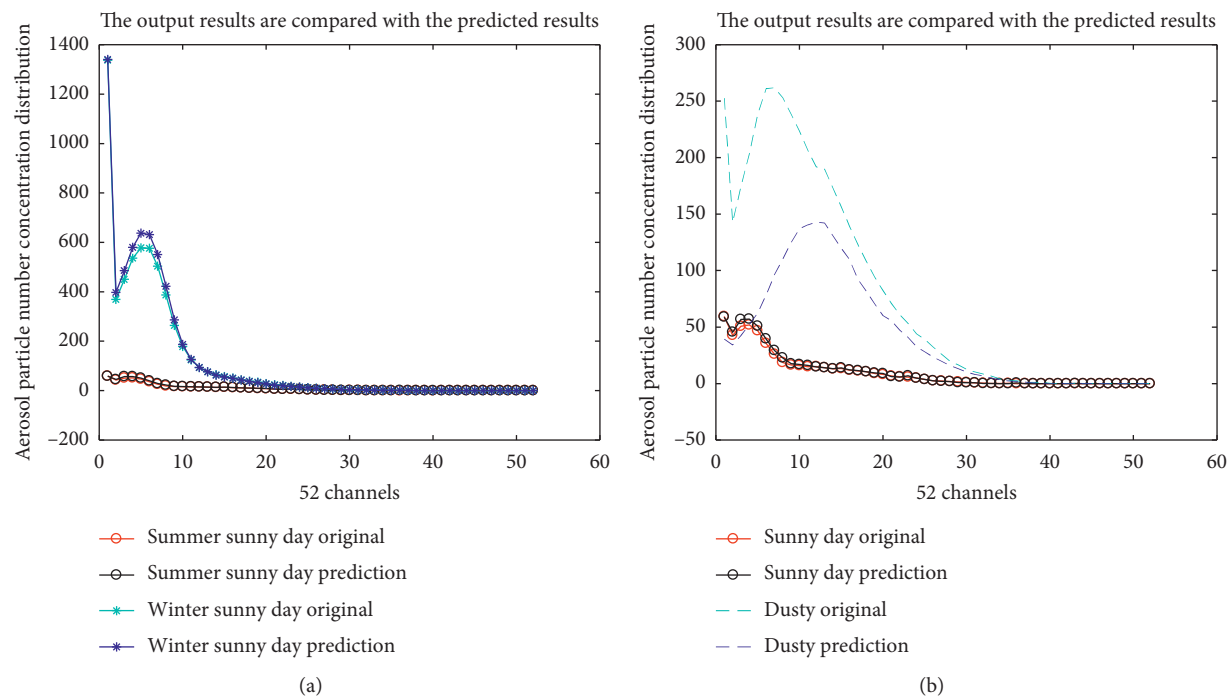


FIGURE 8: The comparison between prediction results and measured results on sunny, winter sunny days, and dusty days based on RBF neural network.

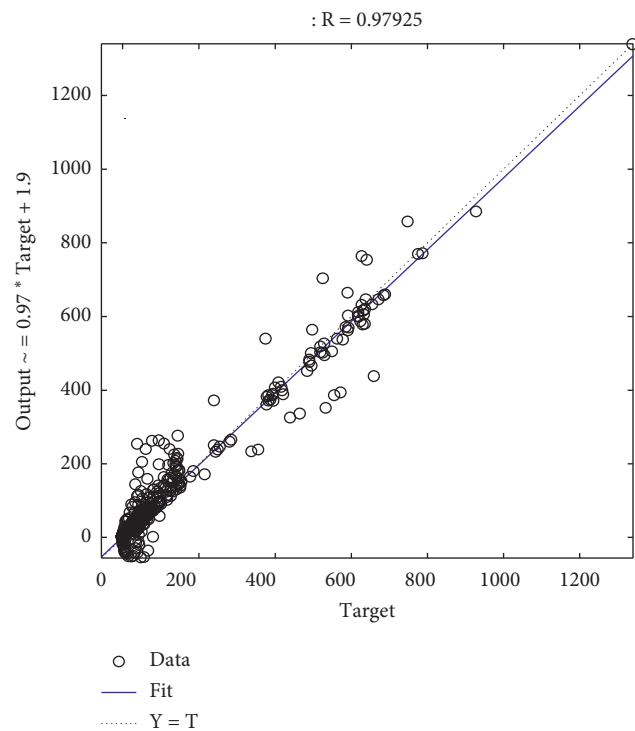


FIGURE 9: The prediction correlation relationship of RBF neural network prediction.

TABLE 2: The preference comparison between BP and RBF neural network.

Prediction model	The correlation coefficient	The average error	RMSE	Time (s)
BP neural network	0.99009	2.3456	5.1769	51
RBF neural network	0.97925	4.7455	11.1557	18

Although the RBF neural network is an efficient feed-forward network and has some advantages, including the best approximation performance, global optimal characteristics that other forward networks do not have, simple structure, and fast training speed, the cost time of BP neural networks is also within an acceptable range for our goal.

5. Conclusions

In this paper, an aerosol PSD prediction model based on the neural networks is established, which is a dual-input single-output prediction mode. The AOD measured by CE-318 and the extinction coefficient obtained by Mie scattering theory are used as the input of the prediction model; also the three weather types of aerosol particle number concentration distribution, summer sunny days, winter sunny days, and spring dusty days, are selected as the output of the prediction model. In order to verify the feasibility of the prediction model, some experiments are performed using BP and RBF neural networks. Compared with the RBF neural network, the BP neural network has better prediction results, including better correlation and smaller errors. However, the prediction time of the BP neural network will be longer, but it also belongs to the acceptable category. In the future research work, we need to continuously improve the accuracy of the prediction model and further reduce the prediction time. We also need to conduct further analysis and research on the aerosol PSD in different seasons and different weather conditions. The research has great significance for inverting the aerosol PSD and further understanding of aerosols' direct effects and indirect effects, as well as the local climate.

Data Availability

The aerosol particle size distribution and concentration data used to support the findings of this study are available from the corresponding author upon request.

Conflicts of Interest

The authors declare that there are no conflicts of interest regarding the publication of this article.

Acknowledgments

This work was supported by the National Natural Science Foundation of China (nos. 61765001 and 61565001), Leading Talents of Scientific and Technological Innovation of Ningxia, Plan for Leading Talents of the State Ethnic Affairs Commission of China, high-level talent selection and training plan of North Minzu University, and Innovation Team of Lidar Atmosphere Remote Sensing of Ningxia.

References

- [1] J. Li, Y. Yin, P. Li, and F. Xu, "Advances in research on mechanism and observation of impacts of aerosol on cloud and precipitation," *Journal of the Meteorological Science*, vol. 34, no. 5, pp. 581–590, 2014.

- [2] W. Dong, "Constrained optimization methods for inversion of aerosol particle size distribution functions," *Chinese Journal of Atmospheric Sciences*, vol. 33, no. 5, pp. 977–981, 2011.
- [3] Y. Tang, Y. Deng, Y. Liu et al., "Research review of remote sensing for atmospheric aerosol retrieval," *Remote Sensing Technology and Application*, vol. 33, no. 1, pp. 25–34, 2018.
- [4] V. Vitale, C. Tomasi, A. Lupi et al., "Retrieval of columnar aerosol size distributions and radiative-forcing evaluations from sun-photometric measurements taken during the clearcolumn (ACE 2) experiment," *Atmospheric Environment*, vol. 34, no. 29–30, pp. 5059–5105, 2000.
- [5] H. Che, X.-Y. Zhang, X. Xia et al., "Ground-based aerosol climatology of china: aerosol optical depths from the china aerosol remote sensing network (CARSNET) 2002–2013," *Atmospheric Chemistry and Physics*, vol. 15, no. 13, pp. 7619–7652, 2015.
- [6] H. Che, X. Xia, H. Zhao et al., "Spatial distribution of aerosol microphysical and optical properties and direct radiative effect from the China aerosol remote sensing network," *Atmospheric Chemistry and Physics*, vol. 19, no. 18, pp. 1843–1864, 2019.
- [7] W. Fan, K. Chen, X. Ling, S. Xun, and C. Yu, "Atmospheric optical characteristics of national climate observation in shouxian county in winter," *Laser & Optoelectronics Progress*, vol. 56, no. 5, Article ID 050101, 2019.
- [8] H. Zhao, *Atmospheric Aerosol Detection and Experimental Research Based on Multiwavelength Lidar and In-Situ Instruments*, Xi'an University of Technology, Xi'an, China, 2017.
- [9] Z. Rao, T. He, D. Hua, and R. Chen, "Remote sensing of particle mass concentration using multi-wavelength lidar," *Spectroscopy and Spectral Analysis*, vol. 38, no. 4, pp. 1025–1030, 2018.
- [10] G. F. Bohren and D. R. Huffman, *Absorption and Scattering of Light by Small Particles*, Wiley, New York, NY, USA, 1983.
- [11] F. Liu and S. Niu, "Optical thickness and size distribution of dust aerosol particles in inner Mongolia," *Journal of Nanjing Institute of Meteorology*, vol. 29, no. 6, pp. 775–781, 2006.
- [12] Y. Wang, S. Fan, and X. Feng, "Retrieval of the aerosol particle size distribution function by incorporating a priori information," *Journal of Aerosol Science*, vol. 38, no. 8, pp. 885–901, 2007.
- [13] D. L. Phillips, "A technique for the numerical solution of certain integral equations of the first kind," *Journal of the ACM (JACM)*, vol. 9, no. 1, pp. 84–97, 1962.
- [14] S. Twomey, "Comparison of constrained linear inversion and an iterative nonlinear algorithm applied to the indirect estimation of particle size distributions," *Journal of Computational Physics*, vol. 18, no. 2, pp. 188–200, 1975.
- [15] G. Ramachandran and D. Leith, "Extraction of aerosol-size distributions from multispectral light extinction data," *Aerosol Science and Technology*, vol. 17, no. 4, pp. 303–325, 1992.
- [16] J. Mao and J. Li, "Retrieval of particle size distribution from aerosol optical thickness using an improved particle swarm optimization algorithm," *Optical Review*, vol. 22, no. 5, pp. 809–818, 2015.
- [17] X. Qin, *Noise Reduction for Lidar Return Signal and the Inversion of Size Distribution of Dust Particles Based on Wavelet Analysis*, North Minzu University, Yinchuan, China, 2017.
- [18] F. Hu and B. Zhang, "Improved algorithm for the retrieval of aerosol optical depth using the sunphotometer CE 318," *Optical Technique*, vol. 33, no. S1, pp. 38–43, 2007.
- [19] Y. Chen, "Discussion on experimental application of lambert-beer law," *Acta Metrologica Sinica*, vol. 6, no. 1, pp. 55–58, 1985.

- [20] C. Matzler, *MATLAB Functions for Mie Scattering and Absorption*, Institut für Angewandte Physik, University of Bern, Münster, Germany, 2002.
- [21] F. Tuo and C. Xu, "Analysis of atmospheric aerosol concentration and particle size by TSI 3321 APS," *Chinese Journal of Radiological Health*, vol. 18, no. 4, pp. 507-508, 2009.
- [22] W. Wang, Q. Guo, and W. Li, "Predictive model based on improved BP neural network and its application," *Computer Measurement & Control*, no. 1, pp. 39-42, 2005.
- [23] W. Wu and J. Wang, "Convergence analysis of the online gradient method for BP neural networks," *Neural Networks*, vol. 12, no. 24, pp. 91-98, 2011.
- [24] J. P. Ren and R. G. Song, "Hardness prediction of 7003 aluminum alloy by gradient descent algorithm in BP artificial neural networks," *Advanced Materials Research*, vol. 217-218, pp. 1458-1461, 2011.
- [25] H. Ai, H. Pan, and Y. Li, "Research on optimization of PM2.5 content prediction in air haze," *Computer Simulation*, vol. 34, no. 1, pp. 392-395, 2017.
- [26] X. Ao, Y. Zheng, Y. Yu, J. Wang, and F. Li, "PM2.5 prediction method based on multiple time series," *Journal of Chongqing Technology and Business University*, vol. 36, no. 2, pp. 41-47, 2019.